The International Journal of Advanced Manufacturing Technology
https://doi.org/10.1007/s00170-026-17895-z

ORIGINAL ARTICLE

A multi-regime thermal source model for laser welding process optimization

Paolo Ferro[1] · Riccardo Rossi[2] · Alessandra Varone[2] · Giuliano Angella[3] · Franco Bonollo[1] · Fabio Bergamini[4]

Received: 12 October 2025 / Accepted: 13 March 2026

Abstract
Industrial laser welding requires rapid parameter optimization, but existing CFD models remain too computationally expensive for practical use. This work addresses this challenge through a calibrated multi-regime thermal source model that enables fast prediction of weld geometry while maintaining engineering accuracy. The model uniquely combines conduction and keyhole welding regimes within a single analytical framework, accounting for beam wobbling and plasma effects. Validated through bead-on-plate experiments on IN625 across industrial-relevant parameters, the approach reduces computational effort significantly compared to fluid dynamics simulations, making it suitable for industrial parameter screening and optimization.

Keywords Laser welding · Wobble effect · Power density distribution function · IN625 · Finite element · Fusion zone

Nomenclature

A_e	laser effective absorptivity
A_m	laser absorption value of a flat metal surface
D [mm^2/s]	thermal diffusivity
d*	normalized melt pool depth
f [mm]	focal length
H [mm]	plate thickness
h_c [W/(m^{2}K)]	heat transfer coefficient
H_m [J/mm^3]	volumetric melting enthalpy of the alloy
K, k	constants
l_{00} [mm]	plasma characteristic attenuation length
l_{02} [mm]	backside characteristic attenuation length
L_{th}*	normalized thermal diffusion length, represented as
OPD [mm]	optical (laser) penetration depth
P [W]	laser power
r_0 [mm]	beam waist at the lens
r_b [mm]	minimum beam waist
r_{wp}[mm]	wobbling equivalent radius (applied to q_{plasma})
r_{wb}[mm]	wobbling equivalent radius (applied to $q_{backside}$)
r_{wl} [mm]	backside wobbling equivalent radius (applied to $q_{laserbeam}$)
v [mm/s]	welding speed
z_f [mm]	laser focus
β_{A_e}	normalized enthalpy computed using A_e
β_{A_m}	normalized enthalpy computed using A_m
η_1	fraction of incident laser power absorbed by the plasma
η_2	fraction of transmitted power contributing to backside heating

✉ Paolo Ferro
paolo.ferro@unipd.it

[1] Department of Management and Engineering, University of Padova, Stradella S. Nicola 3, Vicenza 36100, Italy

[2] Department of Industrial Engineering, University of Rome "Tor Vergata", Via del Politecnico 1, Rome 00133, Italy

[3] Institute of Condensed Matter Chemistry and Technologies for Energy (ICMATE), National Research Council (CNR), Via R. Cozzi 53, Milan 20125, Italy

[4] ENEA, Department for Sustainability-Research Centre of Casaccia, Santa Maria di Galeria, 00123 Rome, Italy

1 Introduction

Laser welding has emerged as a crucial technology in the fabrication and repair of components made from nickel-based alloys [1, 2]. These alloys, known for their exceptional strength, corrosion resistance, and high-temperature

Published online: 30 March 2026

performance, are extensively used in demanding industries such as aerospace [3], power generation, and chemical processing. The precision and control offered by laser welding make it particularly suitable for working with these sophisticated materials, as it helps preserve the critical properties of nickel-based alloys which can be sensitive to thermal cycles [4]. Moreover, laser welding's ability to produce narrow, deep welds with a small heat-affected zone is advantageous in maintaining the microstructure and mechanical properties of these alloys [5, 6]. In repair applications, laser welding offers the potential for localized, controlled material deposition, enabling the restoration of worn or damaged components with minimal impact on surrounding areas [7, 8]. As industries continue to push the boundaries of material performance, the role of laser welding in fabricating and repairing nickel-based alloy components becomes increasingly significant. However, this widespread industrial adoption creates an urgent need for efficient process optimization tools that can reduce experimental costs while ensuring weld quality.

The widespread industrial adoption of laser welding creates a critical need for efficient parameter optimization methodologies. Laser welding of IN625 superalloy is particularly crucial in advanced manufacturing [9, 10], but presents unique challenges that require precise parameter control. Research has focused on the relationship between laser parameters, microstructure evolution, and mechanical properties of IN625 welds [9, 10], while accurate thermal modelling has proven essential for predicting temperature-dependent metallurgical phenomena, residual stress development, and preventing welding defects like porosity and hot cracking [11].

In this context, two main approaches exist in the literature for modelling laser welding processes [12–19]. On one hand, thermo-fluid dynamics (CFD) models, increasingly accessible through methods like Smoothed Particle Hydrodynamics (SPH) [12–14], provide detailed insights into complex phenomena including Marangoni convection, vaporization, and keyhole formation. However, these high-fidelity simulations present prohibitive computational costs for industrial parameter screening and cannot be directly coupled with mechanical calculations for residual stress analysis. The alternative approach utilizes power density distribution functions [15–19] that bypass fluid dynamics to focus on heat input distribution. This method's key advantage lies in its compatibility with finite element codes, enabling subsequent stress and strain calculations essential for Computational Welding Mechanics (CWM). Although these models simplify certain physical aspects, they offer a practical compromise between computational efficiency and predictive capability for weld pool geometry and thermal history - making them particularly valuable for engineering applications where the primary interest lies in predicting weld characteristics and residual stresses rather than detailed fluid dynamics.

To provide context for the proposed model, it is useful to compare the physical basis of different heat source approaches commonly used in laser welding simulation:

- *Surface heat sources*: these models (e.g., Gaussian surface flux) assume that the laser energy is absorbed entirely at the top surface of the workpiece, with heat subsequently transported inward by conduction. While appropriate for conduction-mode welding where the keyhole is absent or shallow, such sources cannot reproduce the deep penetration characteristic of keyhole-mode welding.
- *Conical volumetric heat sources* [20]: These introduce a depth-dependent power distribution, typically with linear or Gaussian decay along the beam axis. The shape parameters (e.g., cone angle, top and bottom radii) are empirically tuned to match experimental fusion zone geometries. However, these parameters lack a clear physical connection to the underlying phenomena and must be recalibrated for each combination of process parameters.
- *Absorptivity-based volumetric models* [21, 22]: Grounded in the Beer-Lambert law, these models use an equivalent optical penetration depth (OPD) calibrated to account for keyhole effects such as multiple reflections and beam trapping. This approach, adopted in recent work by Vanini et al. [21], provides a physically interpretable framework where the OPD can be related to process parameters through scaling laws [17].
- *Multi-source superposition (present model)*: Extending the absorptivity-based approach, our model explicitly accounts for plasma-induced defocusing at the top surface (spherical source) and backside reflections at the bottom surface (second spherical source). This superposition captures the hourglass morphology characteristic of full-penetration keyhole welding, which simpler volumetric models cannot reproduce.

Comprehensive reviews of such existing thermal source models [19] classify them into two main categories: Geometrically Modified Group (GMG) models, such as the double-ellipsoid [15], conical [20], and cylindrical distributions, and Absorptivity Profile Group (APG) models based on radiation transfer or ray-tracing methods. APG models, while physically grounded in beam-material interaction, are inherently incapable of reproducing the characteristic 'hourglass' morphology of full-penetration keyhole welding, as this shape arises from plasma-induced defocusing effects at both the top and bottom surfaces, phenomena not

captured by absorption profiles alone. GMG models could theoretically approximate this hourglass shape through the superposition of multiple sources (e.g., a conical source for penetration depth combined with two spherical sources for the top and bottom regions). However, such approaches suffer from a fundamental limitation: their geometrical parameters must be recalibrated for every combination of process parameters, with no physical correlation linking them to the underlying thermal and fluid-dynamic phenomena.

As noted in [19], even carefully calibrated GMG models frequently underpredict molten pool dimensions unless subjected to numerous trial-and-error iterations. These limitations underscore the need for a modelling approach that combines physical interpretability with predictive capability across a range of process conditions, a gap that the present work aims to fill. Therefore, while analytical thermal models offer computational advantages, current approaches present significant limitations for industrial welding applications. In this scenario, Vanini et al. [21] advanced the field by developing a laser heat source model that eliminates experimental calibration, building upon Ye et al.'s work [22] to analytically derive parameters through in situ optical absorptivity measurements. However, these models primarily address additive manufacturing scenarios and fail to account for the complex morphologies encountered in plate welding applications. Krasnoperov et al. [23] identified four distinct keyhole penetration modes in laser welding, including the fully developed open keyhole that produces characteristic hourglass-shaped fusion zones, a morphology particularly relevant for industrial full-penetration butt welding. Current thermal models cannot accurately reproduce this complex geometry, as they neither account for plasma-induced beam defocusing at both incidence and exit points nor incorporate the effects of laser beam wobbling increasingly used in industrial practice to improve weld quality and gap-bridging capability [24–26]. This represents a critical gap between academic models and industrial needs for comprehensive welding process optimization.

To address these limitations, this work presents a novel multi-regime thermal source model specifically designed for industrial laser welding process optimization. The proposed model introduces a unified analytical framework that captures the essential physics of conduction, closed keyhole, and open keyhole welding regimes through a superposition of three heat source components: laser beam propagation, plasma-induced defocusing, and backside reflection effects. Unlike previous approaches [21, 22], the model explicitly accounts for the hourglass morphology characteristic of open keyhole regime [23] and incorporates beam wobbling effects through analytical modification of power distribution [27]. The hyperparameters governing these phenomena are derived through a combination of established physical relations [22] and experimental calibration, establishing semi-empirical relationships with process variables that enable predictive capability across different welding conditions. By maintaining the computational efficiency of analytical thermal models while significantly expanding their applicability to industrial welding scenarios, this approach provides a practical tool for rapid parameter optimization where multiple regime transitions and complex geometries must be considered.

The remainder of this paper is structured as follows. Section 2 details the experimental methodology, including material specifications, laser welding parameters, and metallographic analysis procedures employed for model validation. Section 3 presents the analytical formulation of the multi-regime thermal source model, describing the three heat source components and their physical basis. The numerical implementation using finite element analysis is also discussed, along with the approach for hyperparameter determination. Section 4 validates the model against experimental results for IN625 alloy across various laser powers and welding speeds, demonstrating its capability to predict fusion zone geometry in different welding regimes. The developed semi-empirical relationships between hyperparameters and process variables are presented and discussed in the context of industrial applicability. Finally, Sect. 5 summarizes the main conclusions and outlines the model's potential for industrial process optimization, while also discussing limitations and future research directions.

2 Materials and methods

Melt run trials were conducted using an IPG ytterbium fiber laser with a nominal power of 4 kW, capable of both continuous and modulated emission. The laser system operates at a wavelength of 1070 nm, with a focused spot size (rb) of 125 µm and a focal depth of ±4.8 mm. The beam radius at the lens (r0) is 13 mm while the focal length (f) is 250 mm. The system's maximum wobbling capability is 2.5 mm at 1 kHz. The laser focusing head is mounted on an ABB 6-axis robotic arm (Fig. 1a) featuring a 2.05 m maximum reach and a 60 kg payload. The welding station includes a clamping system that also serves to supply the inert shielding gas (Fig. 1b). This system consists of a steel base—capable of pre-heating up to 400 °C, and two fixing brackets. These brackets ensure alignment and secure sheets up to 3 mm thick, while simultaneously providing shielding gas along the entire length of the joint.

In the present study, the laser welding process utilized a modulated power output with equal segment durations of 10 ms each, corresponding to a frequency of 50 Hz and a 50% duty cycle. The modulation is calculated as follows:

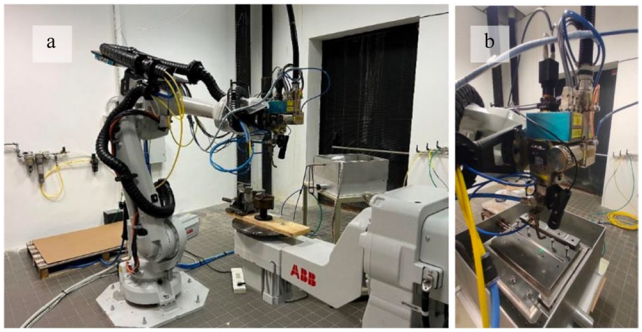

Fig. 1 Experimental laser welding setup, showing the ABB robot arm (**a**) that carries the laser focusing head and clamping (**b**)

$P_1 = \frac{2P_{average}}{1+R}$, $P_2 = RP_1$, where R was set equal to 0.6. Three average power ($P_{average}$) levels were employed: 1700 W, 2000 W, and 2300 W, while welding speeds were varied at 15 mm/s, 20 mm/s, and 25 mm/s to investigate the effect of travel speed on weld characteristics.

The laser focus was positioned on the surface of the workpiece, and beam oscillation (wobbling) was implemented with a circular pattern, featuring a diameter of 0.3 mm and a frequency of 500 Hz. Shielding gas protection was provided using helium, with flow rates of 20 l/min on the top side and 5 l/min on the bottom side of the weld. The welding setup included an ABB robot with a 60 kg payload capacity, 2.05 m reach, and 6 degrees of freedom. Additionally, a welding manipulator with a 250 kg capacity and 2 degrees of freedom was utilized to ensure precise positioning and movement during the welding process. These parameters and equipment specifications were carefully selected to optimize the welding process for the nickel-based alloy, ensuring proper fusion, minimizing defects, and maintaining the material's mechanical properties across a range of power inputs and welding speeds. Figure 1 shows the ABB robotic arm that carries the laser focusing head (a) and the clamping (b).

The material analysed in this study was the nickel-based superalloy Inconel 625, supplied in the form of plates with a thickness of 2.5 mm. The chemical composition is as follows: nickel (bal.), chromium (20-23wt%), molybdenum (8-10wt%), iron (5wt% maximum), niobium (3.15–4.15.15wt%), carbon (0.1wt% maximum), manganese (0.5wt% maximum), silicon (0.5wt% maximum), phosphorus (0.015wt% maximum), sulphur (0.015wt% maximum), aluminium (0.4wt% maximum), titanium (0.4wt% maximum), and cobalt (1wt% maximum).

Following the penetration tests, transverse sections of the various weld beads were obtained by combining different power levels and welding speeds. These cross-sections were carefully prepared using standard metallographic techniques, including cutting, mounting, grinding, and polishing to achieve a mirror-like surface finish. The prepared samples were then examined using optical microscopy to observe and analyse the dimensions and shape of the fusion zone.

3 Laser heat source model

The weld bead morphology observed in the experimental tests indicates that the laser operated in an open keyhole penetration regime [23]. The resulting hourglass-shaped molten zone is particularly challenging to reproduce using a power density distribution function. To the best of the authors' knowledge, no such function has been formulated in the literature, except for conical power distributions whose geometric parameters lack analytical definition, as they are not derived from the underlying physics of the phenomenon [20]. Instead, a model based on the absorption of laser radiation is proposed below, which considers both the beam penetration, and the double divergence induced (in open keyhole penetration regime) at the point of incidence and exit of the laser beam by the formation of plasma (plume) [28, 29]. This plasma defocuses the heat source in both the plate sides and thus generates the hourglass shape of the molten zone. This model can therefore be extended to the closed keyhole penetration regime, by neglecting plasma effects at the beam exit, and to the conduction regime when the applied laser power is sufficiently low.

3.1 Analytical formulation

The heat source model consists of three main components that describe: (i) laser beam propagation, (ii) heat generated by laser-induced plasma on the incident surface, and (iii) a backside heat source accounting for both scattering and plasma-induced heating on the opposite surface, represented in Fig. 2(a).

The laser beam heat source is modelled as a Gaussian beam in cylindrical coordinates and is derived from the spatial evolution of beam intensity along the z-axis, direction of propagation of the beam:

$$q_{laserbeam} = -\frac{dI}{dz} = -\frac{d}{dz}\left(\frac{2A_eP_0}{\pi r_1^2}e^{-2\frac{r^2}{r_1^2}}e^{-\frac{z}{OPD}}\right) = \frac{2A_eP_0}{\pi r_1^2 OPD}e^{-2\frac{r^2}{r_1^2}}e^{-\frac{z}{OPD}} \quad (1)$$

with A_e the effective laser absorptivity, P_0 the power of the beam (different from the laser power in presence of plasma, as explained later), r_1 the beam waist, and OPD the optical penetration depth.

It is important to highlight that when the ratio $z/OPD \to 0$ (i.e., when the optical penetration depth is much larger than the plate thickness), the exponential term can be expanded using a Taylor series, and the equation simplifies to Eq. (5) in [21]. However, to preserve generality

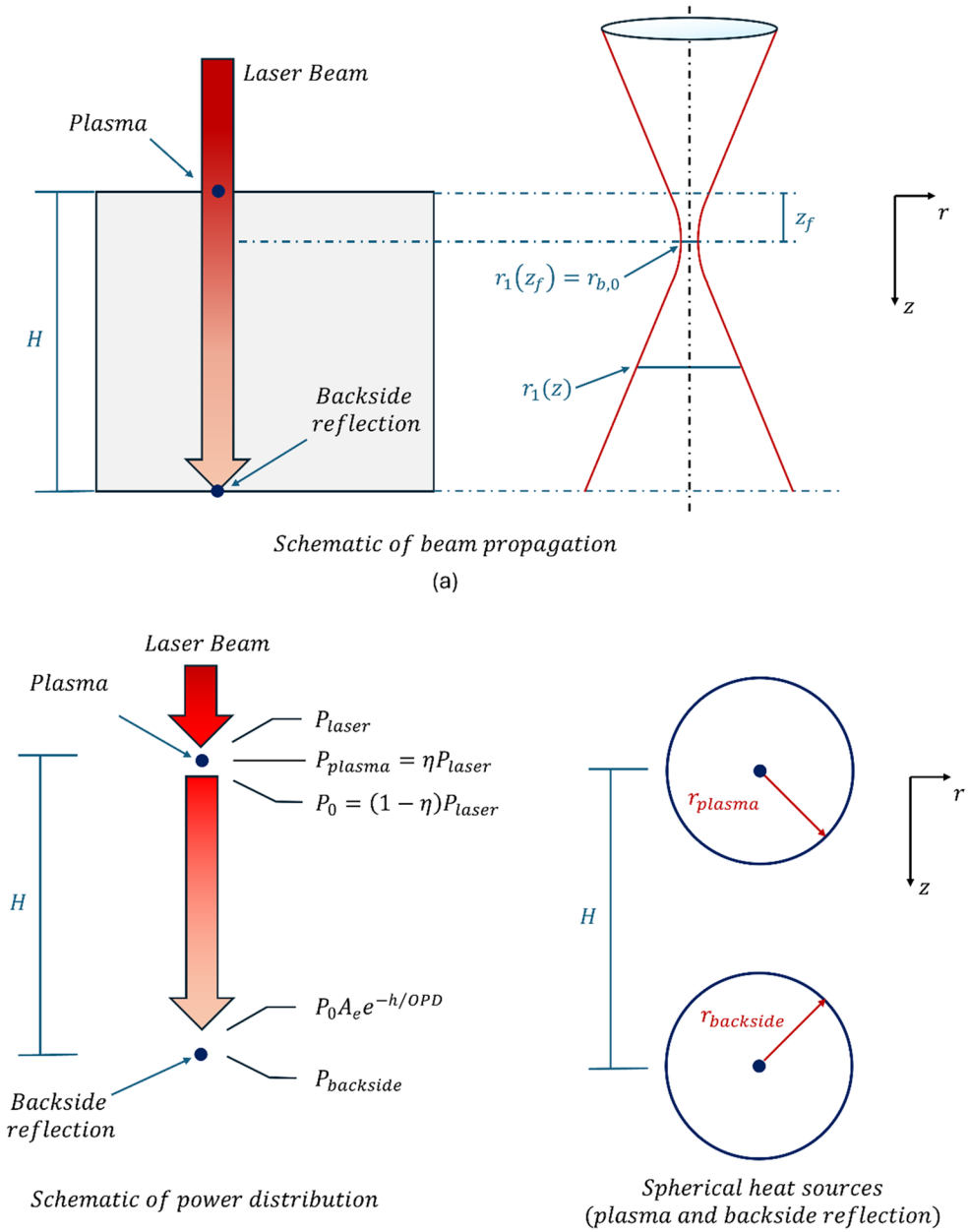

Fig. 2 Schematics of the heat source model

and enable application to different conditions and hyperparameters, the exponential form is retained.

Typically, r_1 is assumed constant. However, this simplification neglects the convergence and divergence of the laser beam, schematically shown on the left side of Fig. 1(a). To address this, r_1 is modelled as a function of z:

$$r_1(z) = \sqrt{\left(\frac{z - z_f}{f}\right)^2 r_0^2 + r_b^2} \tag{2}$$

with f focal length of the lens, z_f the focus position, r_0 the beam waist at the lens and r_b the minimum waist of the beam. Analytically, this introduces a dependency of r_1 on z in Eq. (1), requiring a more complex derivative. However, it can be shown that this results in additional terms proportional to $(z - z_f)/f^2$. Given that typical focal lengths are much greater than the plate thickness, and $(z - z_f)$ is on the order of the plate depth, these terms can be reasonably neglected in a first-order approximation. Moreover, their minimal effects are implicitly captured through the empirical tuning of the model hyperparameters. In the numerical implementation, the beam radius r_1 is treated as a function of the depth coordinate z according to Eq. (2). At each integration point, the local value of $r_1(z)$ is computed and used in Eq. (3) to determine the volumetric heat source distribution.

This ensures that the convergence and divergence of the laser beam are accurately represented throughout the plate thickness. Although the theoretical derivation in Eq. (1) involves a derivative that would generate additional terms proportional to (z-z_f)/f^2, these terms are negligible for typical welding parameters and are not required in the direct implementation of Eq. (3) with z-dependent r_1.

An additional factor to consider is the wobbling effect, which introduces asymmetry into the heat distribution [27]. While this could theoretically require a non-axisymmetric model, the time-averaged effect of the wobble remains axisymmetric [27] and can be incorporated by introducing a wobbling radius, r_{wl} into the heat source expression:

$$q_{laserbeam} = \frac{2A_e P_0}{\pi r_1^2 OPD} e^{-2\frac{(r-r_{wl})^2}{r_1^2}} e^{-\frac{z}{OPD}} \quad (3)$$

The equation above represents the final form of the heat source accounting for both beam divergence and wobble.

It is important to clarify the physical meaning of the Optical Penetration Depth (OPD) used in this model. While the true optical penetration depth for metals at NIR wavelengths is on the order of tens of nanometers, the OPD in our formulation represents an equivalent or effective penetration depth that accounts, in a lumped-parameter manner, for multiple physical mechanisms: (i) multiple reflections within the keyhole, which distribute energy along the depth [14, 17]; (ii) keyhole waveguiding effects; (iii) plasma absorption and isotropic re-emission; and (iv) convective heat transport within the molten pool. This concept of an equivalent OPD is widely adopted in conduction-based thermal modeling of laser welding and additive manufacturing [21, 22, 30], where it is calibrated to reproduce experimentally observed fusion zone geometries. In essence, the OPD is a process-dependent parameter that encapsulates the complex physics of keyhole-mode energy deposition within a computationally efficient conduction-based framework.

The treatment of beam wobbling through a static, time-averaged geometric expansion (parameter r_{wl} in Eq. 3) relies on the assumption that the oscillation frequency is sufficiently high relative to the thermal diffusion timescale of the material. The validity of this approximation can be quantified by comparing the oscillation period (τ_{osc} = 1/f) with the thermal diffusion time constant τ_{th} = L^2/D), where L is a characteristic length scale and D is the thermal diffusivity.

For the present experimental conditions (f=500 Hz, D(IN625) about 7.79 * 10^{-6} m²/s), two relevant length scales can be considered:

- The laser beam radius (r_b = 0.125 mm) gives τ_{th} = 2.0*10^{-3} s, yielding $\tau_{osc}/\tau_{th} \sim 1.0$.
- The melt pool half-width (L_{pool} ~ 1 mm) gives τ_{th} = 0.13 s, yielding $\tau_{osc}/\tau_{th} \sim 0.015 << 1$.

Since the relevant thermal smoothing occurs over the scale of the entire molten pool rather than the instantaneous beam spot, the condition $\tau_{osc}/\tau_{th} << 1$ is satisfied. This indicates that thermal diffusion effectively averages out temperature fluctuations over timescales much shorter than the pool's thermal response time.

This approach is consistent with state-of-the-art wobble laser welding models in the literature. Mukherjee et al. [27] adopt a quasi-steady assumption in their comprehensive CFD study of wobble laser welding of Inconel 740 H, employing a time-averaged power density distribution to successfully predict fusion zone geometries across a range of wobble amplitudes (0.4–1.6 mm) and frequencies (150–411 Hz). They further observe that frequency has minimal impact on fusion zone geometry above 150 Hz, consistent with the thermal diffusion argument presented here.

A general validity criterion for the time-averaged approximation can be expressed as: $f > \frac{D}{L_{pool}^2}$

where L_{pool} is the characteristic melt pool half-width. For typical industrial wobble welding applications with frequencies exceeding 100 Hz, this condition is readily satisfied. At significantly lower frequencies (e.g., f<50 Hz) where τ_{osc} becomes comparable to τ_{th}, the approximation would break down and a transient model would be required to capture periodic fluctuations in pool geometry.

At low laser powers (conduction regime), P_0 is taken to be equal to the total laser power P. However, at higher powers (keyhole regime), a plasma is generated at the incident surface, consuming part of the incoming energy. To account for this, a hyperparameter η_1 is introduced representing the fraction of laser power absorbed by the plasma:

$$P_0 = (1 - \eta_1) P \quad (4)$$

The absorbed plasma energy is re-emitted spherically. Thus, the heat source due to the surface plasma is modelled as:

$$q_{plasma} = \frac{A_e \eta_1 P}{4\pi r_{plasma}^2 l_{00}} e^{-\frac{(r_{plasma} - R_0)}{l_{00}}} \quad (5)$$

with l_{00} the plasma characteristic attenuation length, R_0 a minimum radius used to avoid strong absorption (singularity) in a region where the material is expected to be melted or vaporized, and

$$r_{plasma} = max\left(\sqrt{(r - r_{wp})^2 + (z - z_f)^2}, R_0\right) \quad (6)$$

Compared to a rigorous calculation, this formulation omits a geometric term, which is instead absorbed into the choice of the hyperparameter l_{00}.

A similar heat source is defined for the backside of the plate. When laser power is sufficiently high, a secondary melting region is often observed on the rear surface, approximately symmetric to the front. This is attributed to multiple internal reflections. While full modelling would require a ray tracing approach, this effect is approximated with another spherical source. The laser power transmitted through the plate is given by:

$$P_{backside} = \eta_2 P_0 A_e e^{-H/OPD} \tag{7}$$

where η_2 is the fraction of energy contributing to the backside source and H the plate thickness in the reference system shown in Fig. 2a. The corresponding heat source is:

$$q_{backside} = \frac{A_e P_{backside}}{4\pi r_{backside}^2 l_{02}} e^{-\frac{(r_{backside}-R_0)}{l_{02}}} \tag{8}$$

with l_{02} the backside characteristic attenuation length and

$$r_{backside} = max\left(\sqrt{(r-r_{wb})^2 + (z-H)^2}, R_0\right) \tag{9}$$

It is important to note that l_{00} and l_{02} are not physical penetration depths, but rather characteristic attenuation lengths that govern the spatial decay of the spherical heat sources. They determine the extent of the thermal influence zone of the plasma and backside reflections, respectively. Larger values indicate a more diffuse, wider distribution of energy, while smaller values indicate a more concentrated, localized source. These parameters are empirically calibrated from experimental fusion zone geometries.

The total laser power P is partitioned as follows: a fraction η_1 is absorbed by the plasma and re-emitted spherically (q_{plasma}); the remaining fraction $(1-\eta_1)P$ propagates as the collimated beam (P_0) and contributes to $q_{laserbeam}$. After attenuation through the plate thickness ($e^{-H/OPD}$) and accounting for absorptivity (A_e), the transmitted power is $P_0 A_e e^{-H/OPD}$. Of this transmitted power, a fraction η_2 contributes to the backside spherical source $q_{backside}$. In the present work, $\eta_2$was consistently found to be 1.0 (Table 1), indicating that for full-penetration keyhole welding, all transmitted power contributes to backside heating.

The total heat source is then given by the sum of the three components:

$$q_{total} = q_{laserbeam} + q_{plasma} + q_{backside} \tag{10}$$

Figure 2(b) and (c) illustrate the distribution of power among the three sources and a schematic representation of the spherical heat sources, respectively.

It is important to note that this model is designed to replicate various laser melting conditions without requiring custom heat source formulations. For instance, when the laser power is insufficient to generate plasma, η_1 will be small or zero, effectively eliminating the plasma term. Likewise, if the plasma energy is mostly absorbed near the surface, very little reaches the backside, minimizing the third term. However, this flexibility comes at the cost of introducing several hyperparameters. While some of these have been characterized in prior studies (see next section), others require empirical scaling laws that may vary with laser and material properties. In this work, we propose and examine some of these scaling laws in the results section. Finally, Appendix A illustrates the capabilities of the unified proposed model to capture different laser welding regimes.

3.2 Hyperparameters calculation

In their research, Ye et al. [22] explored the relationship between several key parameters in the context of melt pool dynamics. They introduced the normalized melt pool depth, denoted as d*, which is calculated by dividing the actual

Table 1 Complete collection of parameters used in the model

P [W]	v [mm/s]	l_{00} [mm]	OPD* [mm]	l_{02} [mm]	η_1	r_{wp}= r_{wb} [mm]	r_{wl} [mm]
1700	25	0.35	2.3	0.1	0.2	0.25	0.03
1700	20	0.42	3.64	0.19	0.2	0.33	0.03
1700	15	0.55	6.47	0.45	0.2	0.65	0
2000	25	0.397	2.74	0.16	0.2	0.31	0.03
2000	20	0.485	4.28	0.29	0.27	0.5	0
2000	15	0.65	7.6	0.8	0.15	0.85	0
2300	25	0.45	3.15	0.23	0.2	0.4	0.02
2300	20	0.56	4.93	0.47	0.2	0.58	0
2300	15	0.75	8.76	1.5	0.13	1	0

z_f = 0 mm; f=250 mm, H=2.5 mm, r_b = 0.125 mm, R_0=0.05 mm, r_0=13 mm, η_2=1, k=0.28**

*Eq. (14) ** Eq. (13)

melt pool depth by r_b. This normalized depth was then correlated with two other significant factors: the normalized thermal diffusion length, represented as L^*_{th}, and the normalized enthalpy, β_{A_m}. It's worth noting that the latter parameter, β_{A_m}, was specifically computed using A_m (the laser absorption value of a flat metal surface that for IN625 was found to be equal to 0.27 [22]). L^*_{th} is defined as [21]:

$$L^*_{th} = \sqrt{\frac{D}{r_b v}} \tag{11}$$

where D is the thermal diffusivity [m^2/s], and v is the welding speed. β_{A_m} is given by:

$$\beta_{A_m} = \frac{A_m P}{\pi H_m r_b \sqrt{D r_b v}} \tag{12}$$

where, P is the laser power and H_m (J/m^3) is the volumetric melting enthalpy of the alloy. Finally, the effective absorptivity, A_e, was established through a comprehensive approach involving calorimetry-based measurements of laser energy absorption. This method was applied across an extensive spectrum of laser settings and various alloy compositions. By employing this wide-ranging experimental framework, Ye et al. [22] were able to define A_e as:

$$A_e = k\left(1 - e^{-0{,}66\beta_{A_m} L^*_{th}}\right) \tag{13}$$

with k a constant.

Finally, the normalized melt pool depth is given by [21],

$$d^* = \frac{OPD}{r_b} = K\beta_{Ae} L^*_{th} \tag{14}$$

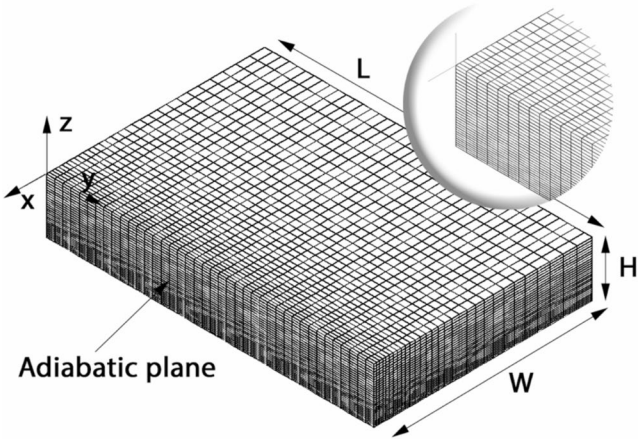

Fig. 3 Mesh of the numerical model with dimensions and reference system (L = 15 mm, W = 10 mm, H = 2.5 mm)

where K is an empirical constant independent of the material and process condition equal to 0.6 [22].

The model proposed in this work introduces several new parameters that enhance its predictive capabilities. Among these are l_{00} and l_{01}, which are designed to model the defocusing of the laser beam as it enters and exits the keyhole (according to open or close keyhole regime). Additionally, the parameters r_{wl}, r_{wp} and r_{wb} are incorporated to account for the effects of wobbling on power density distribution.

It's important to note that these parameters weren't arbitrarily chosen or theoretically derived. Instead, they were obtained through a rigorous process of experimental calibration. This approach ensures that the model is grounded in real-world observations and data. Particularly noteworthy is the development of semi-empirical relationships between these newly introduced parameters and the heat input, represented by the ratio of laser power to welding speed (P/v). These relationships provide valuable insights into how the beam's behaviour and the wobbling effect change under different processing conditions.

The specifics of these semi-empirical relationships, including their formulation and implications, will be elaborated upon in the subsequent section of the paper.

3.3 Numerical model

Following convergence analysis, the optimal mesh configuration for the numerical model is depicted in Fig. 3. Taking advantage of geometrical and loading symmetry, the model reproduces one half of plate, where the penetration test is carried out, employing 39,600 8-node brick finite elements. To accurately resolve the steep thermal gradients inherent in high-power density welding processes, a graduated density mesh was implemented. Boundary conditions were applied as follows: an adiabatic condition was imposed on the symmetry plane, while convective heat transfer (with a coefficient h_c=25 $W/(m^2 \cdot K)$ [31]) and radiative heat loss (with surface emissivity set to 0.7 for Stefan–Boltzmann radiation) were applied to the remaining external surfaces. Temperature-dependent physical and thermal material properties, as detailed in Appendix B, were incorporated into the model.

4 Results and discussion

4.1 Three-dimensional thermal field and fusion zone prediction

Figure 4 shows the 3D representation of the thermal field calculated for $P_{average}$ = 2000 W and v = 25 mm/s,

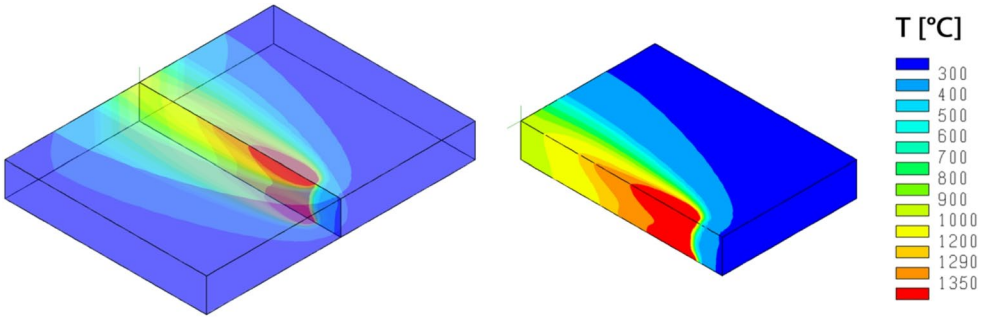

Fig. 4 Two different 3D representations of the thermal field obtained with $P_{average}$ = 2000 W and v = 25 mm/s. The colour scale indicates temperature in °C, with intense red corresponding to T ≥ 1350 °C (liquidus, fully molten zone) and the adjacent band representing temperatures between 1290 °C (solidus) and 1350 °C (mushy zone)

demonstrating the model's capability to capture the complete fusion zone geometry. The red-coloured zone represents the 3D dimensions and shape of the fusion zone (FZ), while the orange zone represents the material between the solidus and liquidus temperatures, highlighting the extent of the mushy zone. This comprehensive thermal visualization provides industrial engineers with immediate insight into the expected weld morphology and thermal distribution, essential for predicting potential defect-sensitive regions and optimizing process parameters.

4.2 Experimental validation across industrial process window

The model's predictive capability was systematically validated against experimental results across the industrial process window. Figures 5, 6 and 7 present the comparative analysis between simulated and experimental fusion zone profiles for laser powers of 1700 W, 2000 W, and 2300 W, respectively, each at welding speeds of 15 mm/s, 20 mm/s, and 25 mm/s.

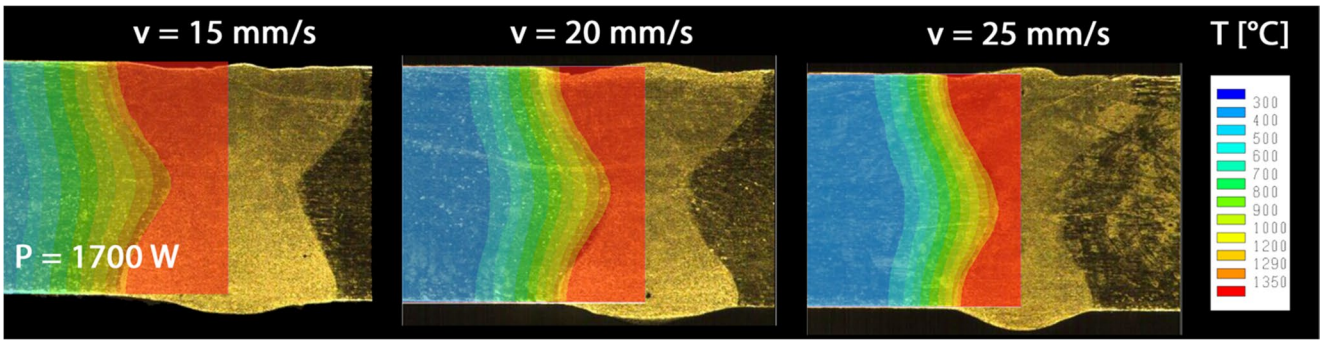

Fig. 5 FZ shape and dimension as a function of welding speed (v) and constant power (P = 1700 W). The colour scale indicates temperature in °C, with intense red corresponding to T ≥ 1350 °C (liquidus, fully molten zone) and the adjacent band representing temperatures between 1290 °C (solidus) and 1350 °C (mushy zone). The experimental fusion zone profile (optical micrograph) is superimposed for comparison

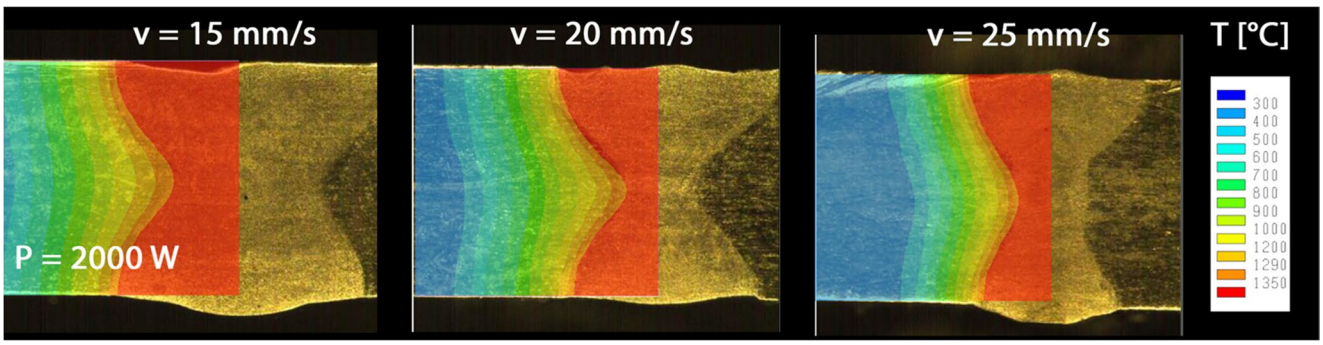

Fig. 6 FZ shape and dimension as a function of welding speed (v) and constant power (P = 2000 W). The colour scale indicates temperature in °C, with intense red corresponding to T ≥ 1350 °C (liquidus, fully molten zone) and the adjacent band representing temperatures between 1290 °C (solidus) and 1350 °C (mushy zone). The experimental fusion zone profile (optical micrograph) is superimposed for comparison

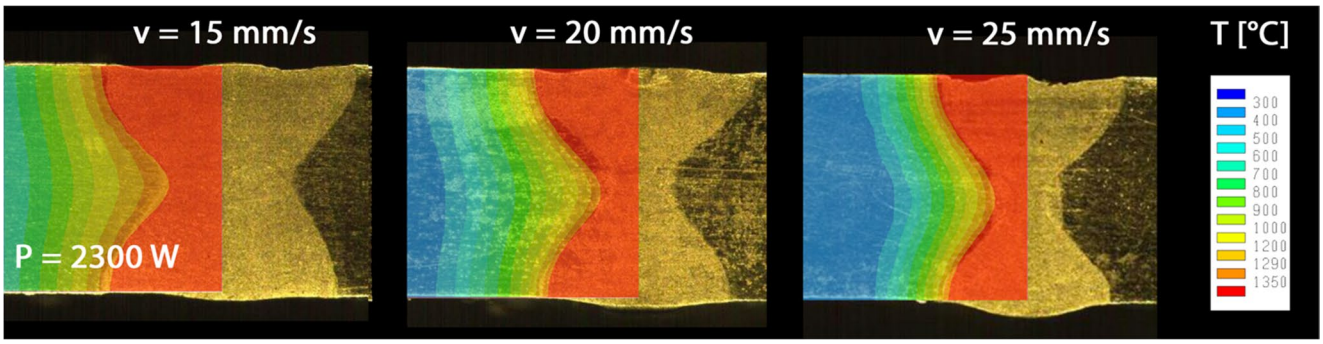

Fig. 7 FZ shape and dimension as a function of welding speed (v) and constant power (P=2300 W). The colour scale indicates temperature in °C, with intense red corresponding to T≥1350 °C (liquidus, fully molten zone) and the adjacent band representing temperatures between 1290 °C (solidus) and 1350 °C (mushy zone). The experimental fusion zone profile (optical micrograph) is superimposed for comparison

The visual superposition demonstrates exceptional agreement between predicted and experimental fusion zone profiles across all parameter combinations. The model achieves complete morphological correspondence, successfully reproducing the characteristic hourglass shape, penetration profile, and key geometrical features essential for industrial quality assessment.

Quantitative analysis using binary overlap methodology confirms an average overlap exceeding 92% between experimental and predicted fusion zones across all test cases. The model consistently predicts complete penetration when observed experimentally and accurately captures the critical weld width at both top and bottom surfaces, key parameters for structural integrity assessment in industrial applications. This level of agreement demonstrates the model's suitability for process optimization, where predicting correct fusion zone morphology and ensuring complete penetration are paramount.

The validation covers the keyhole-dominated regimes, with the model accurately capturing the evolution of fusion zone geometry with increasing power and decreasing welding speed. Particularly noteworthy is the successful reproduction of the open keyhole regime's characteristic morphology, including the plasma-induced defocusing effects at both top and bottom surfaces.

4.3 Industrial calibration methodology

The calibration of hyperparameters governing the multi-regime model reveals systematic relationships with process variables that enhance the model's utility for industrial applications. As summarized in Table 1, the parameters can be categorized into three groups: process-dependent (power, welding speed), laser-specific (focal length, beam waist, focus position), and geometric (plate thickness). The hyperparameters were determined through a hybrid approach, with some calculated using established physical relationships (Eqs. 11–14) for effective absorbance (A_e) and beam penetration (OPD), confirming the validity of previous works by Ye et al. [22] and Vanini et al. [21], while others were calibrated experimentally to capture phenomena specific to industrial welding conditions.

Notably, systematic relationships emerge between key hyperparameters and heat input (P/v). The plasma equivalent penetration length follows a linear relationship:

$$l_{00} = A \bullet \frac{P}{v} + B \tag{15}$$

where A=0.0047 [mm^2/J] and B=0.0187 [mm]. The backside equivalent penetration length exhibits exponential dependence:

$$l_{02} = Me^{N\frac{P}{v}} \tag{16}$$

where M=0.013 mm and N=0.03 [mm/J]. Similarly, the wobbling parameters show linear correlation with heat input:

$$r_{wb} = r_{wp} = F \bullet \frac{P}{v} + G \tag{17}$$

where F=0.093 [mm^2/J] and G = −0.425 [mm].

It is important to emphasize that the semi-empirical relationships presented in Eqs. (15–17), along with their specific coefficients (A, B, M, N, F, G), are not proposed as universal physical laws. They were derived under well-defined experimental conditions: IN625 alloy, plate thickness H=2.5 mm, circular wobbling pattern with diameter 0.3 mm and frequency 500 Hz, and power modulation settings of 50 Hz with R=0.6. These coefficients are valid strictly within this domain. For applications involving different materials, thicknesses, or wobbling parameters, recalibration following the methodology outlined in this work is required. The primary contribution of this study is therefore the physically interpretable modelling framework and the

systematic calibration methodology, which are transferable to new conditions, rather than a fixed set of numerical constants.

These relationships have clear physical justification: increasing heat input (P/v) represents higher energy deposition per unit length, naturally leading to greater equivalent penetration depths and expanded wobbling effects as more material undergoes melting/vaporization. Figure 8 illustrates the excellent agreement between calibrated parameters and the interpolation curves from Eqs. (15–17), demonstrating the consistency of these relationships across the industrial process window.

To further assess the generalizability of the proposed modeling framework, additional validation was performed on a different nickel-based superalloy, Inconel 718 (IN718). Bead-on-plate laser welding trials were conducted on IN718 plates of thickness 2.55 mm using a comparable range of laser powers (1700–2300 W) and welding speeds (15–25 mm/s), with the same wobbling parameters (circular pattern, 0.3 mm diameter, 500 Hz). The model was calibrated following the identical procedure described for IN625, with hyperparameters adjusted to fit the experimentally observed fusion zone morphologies Fig. 9 (a) presents a comparison between the experimental and simulated fusion zone profiles for IN718. Table 2 summarizes the complete set of process parameters and corresponding calibrated hyperparameters for the IN718 validation trial.

While the accurate prediction of fusion zone geometry (Figs. 5, 6, 7 and 9a) provides indirect validation of the overall heat input distribution, a more direct assessment of the model's thermal accuracy is obtained by comparing predicted temperatures with experimental measurements. During the welding trials, K-type thermocouples were embedded at various distances from the weld centerline to record the thermal cycles and, in particular, the peak temperatures reached during the process.

Figure 9(c) presents a comparison between the experimentally measured peak temperatures and those predicted

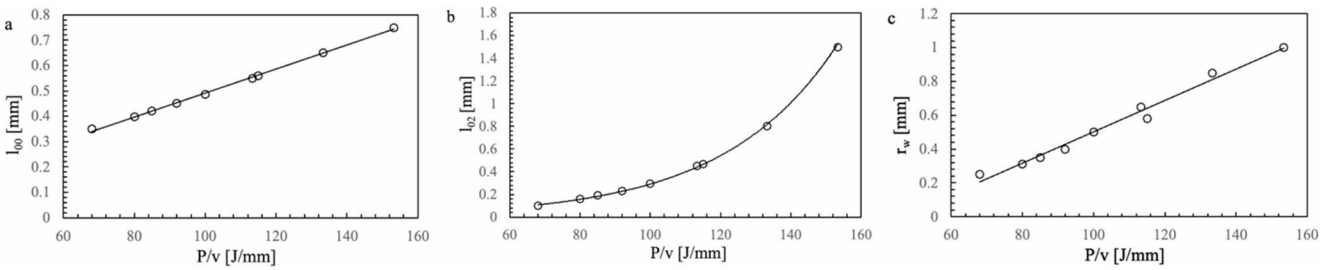

Fig. 8 Hyper-parameters modelling the top and bottom divergence of the fusion zone (l_{00} (**a**), l_{02} (**b**)) and the wobbling effect (r_{wp} and r_{wb} (**c**)): points are calibrated parameters (Table 1), continuous lines are given by Eqs. (15–17), respectively

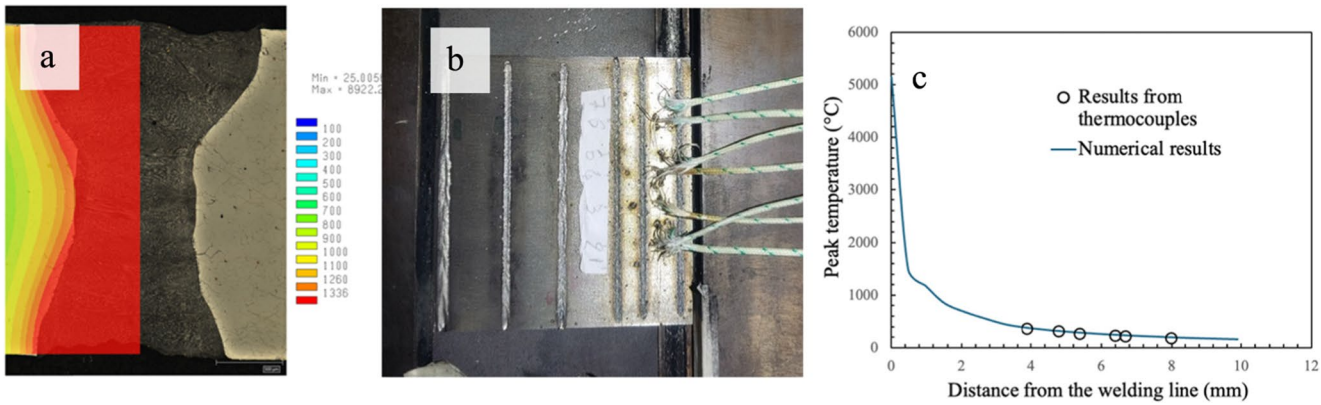

Fig. 9 Numerical and experimental results of laser welding applied to IN718: (**a**) comparison between predicted and experimental shape of FZ; (**b**) picture of thermocouples layout; (**c**) comparison between experimental and numerical peak temperature as a function of the distance from the weld centerline (process and hyperparameters are collected in Table 2)

Table 2 Process parameters and hyperparameters used in the model

P [W]	v [mm/s]	l_{00} [mm]	OPD [mm]	l_{02} [mm]	η_1	η_2	$r_{wp} = r_{wb}$ [mm]	r_{wl} [mm]	Ae
2640	33	0.40	3.00	0.18	0.2	0.1	0.25	0.025	0.40

$z_f = 0$ mm; f = 250 mm, H = 2.55 mm, $r_b = 0.125$ mm, $R_0 = 0.05$ mm, $r_0 = 13$ mm

by the numerical model as a function of lateral distance from the weld centerline. The experimental conditions correspond to $P = 2640$ W, v = 33 mm/s. The numerical curve is extracted from the simulated thermal field at the mid-length of the weld.

The results demonstrate excellent agreement across the entire measurement range (distances from 3.9 mm to 8.9 mm). The experimental data points fall almost exactly on the numerically predicted curve, with an average relative error below 5% and a coefficient of determination $R^2 > 0.98$. This quantitative validation confirms that, despite the neglect of fluid dynamics phenomena such as Marangoni convection, the model accurately captures the thermal field in the region outside the fusion zone—i.e., in the Heat Affected Zone (HAZ) and base material.

This finding warrants further discussion, as it might seem counterintuitive. Convective heat transport within the molten pool undoubtedly affects internal temperature distributions, and if internal gradients were substantially altered, this could in principle influence the heat flux entering the solid and thus modify HAZ thermal histories. However, several factors explain why a conduction-based model with calibrated parameters succeeds in predicting HAZ temperatures:

1. *Compensation through calibration*: The hyperparameters (l_{00}, l_{02}, h_1, etc.) are calibrated to reproduce the experimentally observed *fusion zone geometry*. Since the pool geometry constitutes the boundary condition that determines heat flow into the solid, matching it correctly ensures that the *total* heat flux entering the HAZ is accurate. The calibration process implicitly embeds the integrated effect of convection on pool shape.
2. *Thermal smoothing in the solid*: Temperature gradients in the HAZ are governed by heat diffusion from the pool boundary. Even if internal pool gradients differ between a conduction and a convection model, diffusion in the solid tends to smooth out differences over distances comparable to the thermal diffusion length. For the length scales of interest in HAZ prediction (hundreds of micrometers to millimeters), this smoothing effect is significant.
3. *Direct experimental validation*: Ultimately, the thermocouple measurements provide the most robust evidence. If the neglected convection were causing significant errors in HAZ thermal histories, systematic deviations would be expected between predicted and measured peak temperatures, particularly at locations close to the fusion boundary (3.9 mm distance), where the influence of pool dynamics should be strongest. The observed agreement (error < 5%) confirms that such errors are minimal for this material and process window.

These results are consistent with findings in the literature. Mukherjee et al. [27], employing a full CFD model including Marangoni convection for wobble laser welding of Inconel 740 H, obtained fusion zone geometries remarkably similar to those predicted by the present conduction-based approach. This suggests that for nickel-based superalloys under keyhole conditions, the primary determinant of pool shape is the energy distribution from the beam and keyhole dynamics, with Marangoni flow playing a secondary role in modifying the final pool outline.

The thermocouple validation provides confidence that the model is suitable for engineering applications requiring HAZ prediction (e.g., phase transformations, grain growth) and residual stress analysis for IN625 and similar nickel-based alloys under the investigated process conditions.

However, certain limitations should be acknowledged:

- *Materials with strong Marangoni effects*: In alloys where surface tension gradients are particularly pronounced (e.g., steels with sulfur impurities), Marangoni convection can dramatically alter pool shape and internal temperatures. For such materials, a conduction-only model would require case-specific recalibration that might not generalize across a wide process window.
- *Extremely high Peclet number regimes*: In cases where convective transport overwhelmingly dominates (very low welding speeds or materials with very low thermal diffusivity), the approximation may become less accurate.
- *Internal pool phenomena*: The model cannot capture phenomena that depend on internal fluid flow patterns, such as solute redistribution, pore migration, or the formation of certain solidification defects. For such analyses, a full CFD approach remains necessary.

For the intended industrial application (i.e.: rapid parameter screening, process optimization, and residual stress prediction in IN625 components) the conduction-based approach with experimentally validated thermal fields provides an optimal balance between accuracy and computational efficiency.

These results yield two significant insights. First, the structural robustness of the model is confirmed: the superposition of laser beam propagation, plasma-induced defocusing, and backside reflection effects provides a physically sound representation of the keyhole welding process that extends beyond a single material. Second, as expected, the numerical values of the hyperparameters and their correlation coefficients are material-dependent. The coefficients required to fit IN718 fusion zones differ from those reported for IN625 in Table 1, reflecting variations in key material properties such as effective absorptivity (A_e), thermal

diffusivity (D), and melting enthalpy (H_m). This underscores that while the modelling framework is universally applicable, the semi-empirical relationships expressed in Eqs. (15–17) must be recalibrated for each specific material and set of process conditions.

Consequently, the primary contribution of this work is not a set of universal constants, but rather a robust and transferable methodology for developing predictive thermal source models. For any new material, plate thickness, or wobbling configuration, the same calibration procedure—requiring only a limited number of bead-on-plate experiments—can be employed to establish material- and process-specific correlations. This positions the model as a practical tool for industrial parameter optimization across a wide range of applications.

A theoretical consideration of the influence of plate thickness on the backside parameter l_{02} is warranted. Physically, l_{02} represents the spatial extent of the thermal influence zone generated by backside reflections and plasma re-emission at the keyhole exit. For a fixed heat input, increasing plate thickness (H) introduces two competing effects. First, the transmitted power $P_{backside}$ (Eq. 7) decreases exponentially with H/OPD, reducing the intensity of the backside source. Second, a thicker plate may promote a more fully developed keyhole with altered internal reflection patterns, potentially concentrating energy delivery to the bottom surface. In the limit of very thin plates ($H \to 0$), the backside source would merge with the primary laser source, and $l_{02} \to 0$. In the opposite limit of very thick plates where full penetration is not achieved, the backside source vanishes entirely. Between these extremes, l_{02} is expected to exhibit a non-monotonic or saturating behaviour, likely reaching a maximum at some intermediate thickness where keyhole stability and internal reflections optimize energy transfer to the bottom surface. While a detailed experimental investigation of this thickness dependence lies beyond the scope of the present work, the model's structure is inherently capable of incorporating such correlations once sufficient data become available. This represents a promising direction for future research aimed at extending the model's generalizability across different workpiece geometries.

It should also be noted that the parameter h_1 (fraction of incident laser power absorbed by the plasma) is a purely empirical fitting parameter in the current model. Its values, reported in Table 1, were determined by iterative calibration to minimize the discrepancy between predicted and experimental fusion zone geometries. Direct measurement or first-principles prediction of h_1 is extremely challenging due to the complex physics of laser-plasma interaction; therefore, empirical calibration represents a practical approach for engineering applications.

The semi-empirical approach represents a pragmatic solution for incorporating complex phenomena that present significant analytical challenges. These parameters encompass not only the fluid dynamic effects induced by wobbling but also those resulting from power modulation - employed in our experimental trials to reduce gaseous porosity risk - and intricate optical behaviours within the keyhole. Specifically, the established relationships are valid for the material properties, wobbling parameters (0.3 mm diameter, 500 Hz), and power modulation settings (50 Hz, $R = 0.6$) used in the experimental tests.

This methodology represents the most reasonable compromise given the system complexity, allowing incorporation of phenomena resistant to pure analytical modelling while maintaining foundation in physical principles. It strikes an optimal balance between theoretical understanding and practical applicability, enabling the model to capture essential behaviours observed in industrial welding conditions. The approach provides industry practitioners with a calibrated framework that reliably predicts weld geometry across the process window, without requiring excessive computational resources or analytical complexity that would hinder practical implementation.

4.3.1 Discussion on the range of validity and saturation behaviour

It is important to note that the exponential relationship proposed for l_{02} (Eq. 16) is strictly valid within the experimental range investigated in this study (P/v from 68 J/mm to 153 J/mm for IN625). From a physical standpoint, the backside melt pool width, and consequently the parameter l_{02}, cannot increase indefinitely with heat input. At sufficiently high P/v values, several constraints impose an upper bound:

- *Geometric limitations*: the maximum weld width is ultimately limited by the plate dimensions.
- *Energy conservation*: the power available for backside heating, $P_{backside}$ (Eq. 7), reaches a finite maximum as P increases.
- *Keyhole stability*: at very high energy inputs, the keyhole becomes unstable, leading to defects such as drop-out or excessive spatter, and the hourglass morphology itself may no longer be maintained.

Therefore, beyond the calibrated range, the growth of l_{02} is expected to slow and eventually saturate, approaching an asymptotic maximum value l_{02}^{max}. A more complete physical description would involve a saturating function (e.g., sigmoidal or exponential approach to a limit). However, determining the saturation behaviour would require experimental data at heat inputs outside the stable welding window

for 2.5 mm thick IN625 plates, which were deliberately avoided in this study. For industrial applications within the stable process window, the exponential correlation provides an accurate and convenient description within its range of validity, and extrapolation beyond this range is not recommended without additional experimental validation.

5 Conclusions

This study has presented a multi-regime thermal source model specifically developed for industrial laser welding process optimization. The main contributions and findings can be summarized as follows:

1. *Industrial-Oriented Formulation*: the proposed model provides a computationally efficient alternative to high-fidelity CFD simulations, enabling rapid prediction of weld geometry across conduction, closed keyhole, and open keyhole welding regimes. This addresses a critical industrial need for practical optimization tools that balance accuracy with computational practicality.
2. *Comprehensive Regime Coverage*: through the superposition of three heat source components - laser beam propagation, plasma-induced defocusing, and backside reflection - the model successfully captures complex fusion zone morphologies, including the characteristic hourglass shape of open keyhole regime that previous analytical approaches could not reproduce.
3. *Experimental Validation for Industrial Parameters*: the model was validated through bead-on-plate experiments on IN625 alloy across industrially relevant laser powers (1700–2300 W) and welding speeds (15–25 mm/s), demonstrating robust predictive capability for fusion zone geometry under varying process conditions.
4. *Practical Calibration Framework*: semi-empirical relationships were established between key hyperparameters and heat input (P/v), providing a systematic approach for model calibration that can be adapted to different industrial scenarios while maintaining physical interpretability.
5. Demonstrated Generalizability: the model's structural robustness was further validated through application to IN718 alloy. This confirms that while the numerical coefficients of the semi-empirical correlations are material-dependent, the underlying modelling framework and calibration methodology are transferable to different nickel-based superalloys. This positions the approach as a versatile tool for industrial application, requiring only a limited set of calibration experiments for each new material or process configuration.

Limitations and Industrial Outlook: while the model demonstrates significant value for parameter screening and optimization, its current calibration is specific to IN625 and the tested wobbling parameters. Future work will focus on extending the validation to other materials and thicknesses, developing more generalized calibration protocols, and exploring integration with machine learning approaches for enhanced predictive capability across broader process windows. The model's computational efficiency makes it particularly suitable for industrial digital twin applications and rapid process development cycles.

Appendix A

The heat source model developed in this work comprises three distinct terms which, through appropriate tuning of the associated hyperparameters, can reproduce various welding regimes, ranging from conduction to closed and open keyhole modes. This appendix section aims at illustrating how the model can replicate different heat source by simply changing some of the hyperparameters.

The first example, shown in Figure 10, illustrate the three heat sources (laser, plasma and backside reflection) and the resulting one. In this case, the laser power is so large that it is expected to generate a strong plasma radiation and backside reflections.

By tuning the hyperparameters, different heat sources are replicated. Figure 11 shows four key heat sources: the first, in the left, replicates a conduction regime, where the laser slightly penetrates the material and most of the laser energy is deposited in the incident surface. This has been achieved simply reducing the equivalent OPD. The second case, in the middle left, represents a close keyhole regime without wobbling. The laser beam strongly penetrates plate, leading to deep melting shapes. The effect of adding a wobbling effect on the heat source is illustrated in the middle right plot. It has to be noted that the axis, where the heat power is small because of the analytical formulation, always reach the melting thanks to the thermal diffusivity of the material. The last case, illustrated in the right, shows a heat source for an open

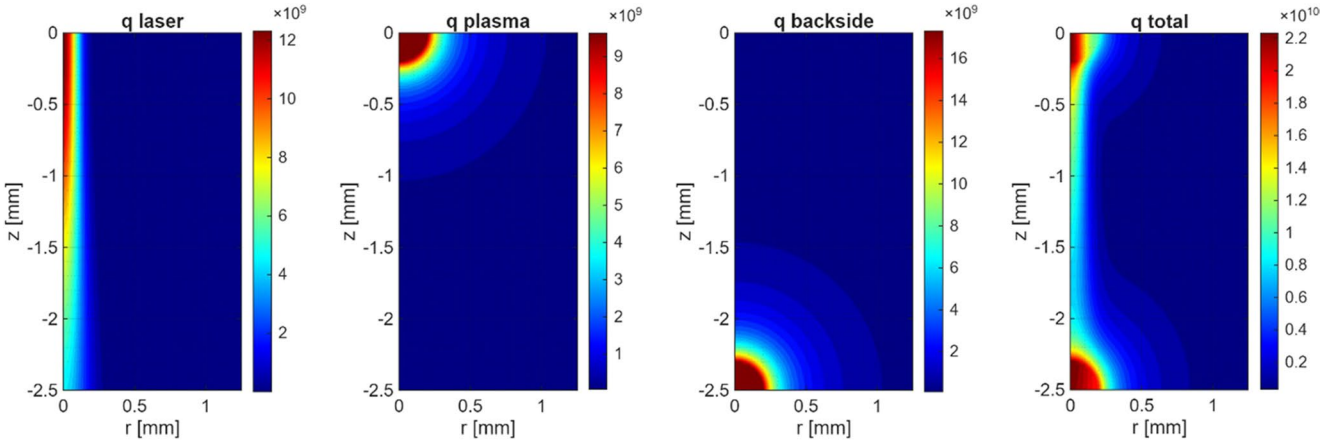

Fig. 10 An example showing the three heat sources (laser, plasma, and backside) and the resulting one

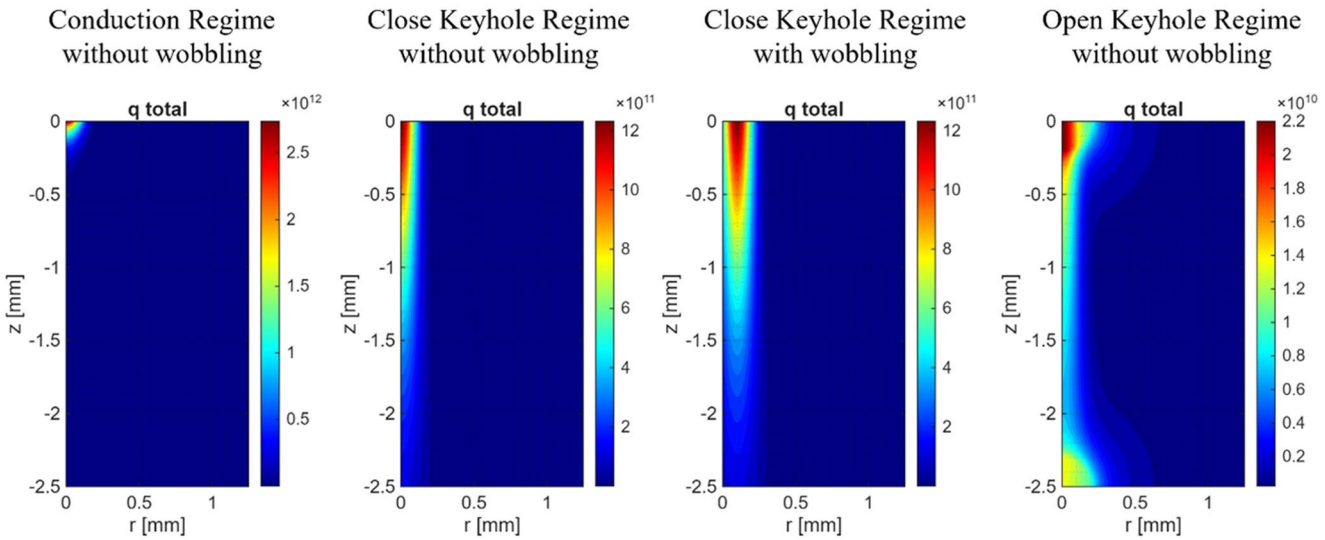

Fig. 11 Four heat sources from our model obtained changing three hyperparameters (laser power P, equivalent OPD, and wobbling radius r_w)

keyhole case, where the power is considered to be so high to generate strong plasma radiation and backside reflection, leading to the typical hourglass shape similar to the melting shape observed in experimental cases. In Table 3, the most relevant hyperparameters for these four cases are illustrated.

Table 3 Hyperparameters used for generating the four regimes

	Laser Power P [W]	OPD [mm]	Wobbling radius r_w [mm]
Conduction regime without wobbling	10 W	0.1 mm	0.0 mm
Close keyhole regime without wobbling	100 W	2.0 mm	0.0 mm
Close keyhole regime with wobbling	100 W	2.0 mm	0.1 mm
Open keyhole regime without wobbling	5000 W	10.0 mm	0.0 mm

Appendix B

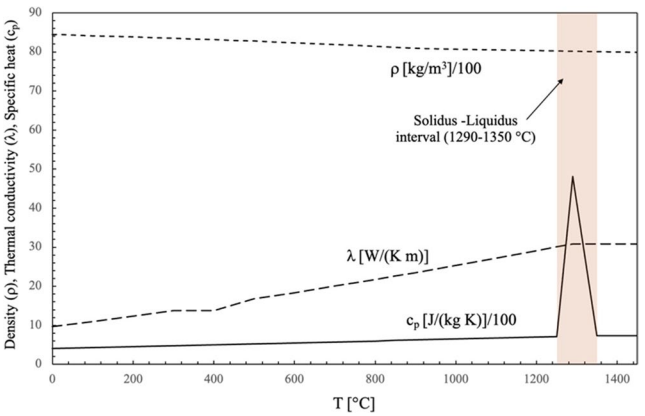

Fig. 12 Physical and thermal material properties of IN625 as a function of temperature

Table 4 IN625 material parameters used to compute the hyperparameters (Eqs. 11–14). They are, for simplicity, assumed constant and set to their values at the liquidus temperatur

Specific Heat (J/(kg °C)	731
Thermal conductivity (W/(mm °C)	0.03
Density (kg/mm^3)	8.44 10^{-6}
Liquidus temperature (°C)	1350
A_m	0.27 [13]
Melting Enthalpy (Hm) (J/mm^3)	7.985 [13]
Thermal diffusivity (mm^2/s)	7.79 [13]

Appendix C: complete derivation of the volumetric heat source and order-of-magnitude analysis of neglected terms

The heat source model is derived from the spatial evolution of laser intensity along the beam propagation direction (z-axis). Starting from the intensity distribution of a Gaussian beam:

$$I(r,z) = \frac{2A_eP_0}{\pi r_1(z)^2} exp(-2\frac{r^2}{r_1(z)^2}) exp(-\frac{z}{OPD}) \tag{C.1}$$

where $r_1(z)$ is the depth-dependent beam radius given by Eq. (2). The volumetric heat source is defined as the negative gradient of intensity:

$$q_{laserbeam} = -\frac{dI}{dz} = -\frac{\partial I}{\partial z} - \frac{\partial I}{\partial r_1}\frac{dr_1}{dz} \tag{C.2}$$

Computing the partial derivatives:

$$\frac{\partial I}{\partial z} = -\frac{2A_eP_0}{\pi r_1^2 OPD} exp(-2\frac{r^2}{r_1^2}) exp(-\frac{z}{OPD}) \tag{C.3}$$

$$\frac{\partial I}{\partial r_1} = \frac{2A_eP_0}{\pi} exp(-\frac{z}{OPD}) \left(-\frac{2}{r_1^3} + \frac{4r^2}{r_1^5}\right) exp(-2\frac{r^2}{r_1^2}) \tag{C.4}$$

From Eq. (2), the derivative of r_1 with respect to z is:

$$\frac{dr_1}{dz} = \frac{(z-z_f)r_0^2}{f^2 r_1(z)} \tag{C.5}$$

Substituting Eqs. (C.3)-(C.5) into Eq. (C.2) yields the complete expression:

$$q_{laserbeam} = \frac{2A_eP_0}{\pi r_1^2 OPD} e^{-2\frac{r^2}{r_1^2}} e^{-\frac{z}{OPD}} + \frac{2A_eP_0}{\pi} e^{-\frac{z}{OPD}} \left(\frac{2}{r_1^3} - \frac{4r^2}{r_1^5}\right) \frac{(z-z_f)r_0^2}{f^2 r_1} e^{-2\frac{r^2}{r_1^2}} \tag{C.6}$$

The first term corresponds to the expression used in Eq. (3). The second term represents the contribution from the depth-dependence of the beam radius. To justify neglecting this term in the theoretical derivation, an order-of-magnitude analysis is performed by taking the ratio between the two terms:

$$\frac{TermII}{TermI} = \frac{\frac{2A_eP_0}{\pi} e^{-\frac{z}{OPD}} \left(\frac{2}{r_1^3} - \frac{4r^2}{r_1^5}\right) \frac{(z-z_f)r_0^2}{f^2 r_1} e^{-2\frac{r^2}{r_1^2}}}{\frac{2A_eP_0}{\pi r_1^2 OPD} e^{-2\frac{r^2}{r_1^2}} e^{-\frac{z}{OPD}}} = \frac{\left(\frac{2}{r_1^3} - \frac{4r^2}{r_1^5}\right) \frac{(z-z_f)r_0^2}{f^2 r_1}}{\frac{1}{r_1^2 OPD}} = OPD\left(\frac{2}{r_1} - \frac{4r^2}{r_1^3}\right) \frac{(z-z_f)r_0^2}{f^2 r_1} = \frac{OPD}{f}\frac{(z-z_f)}{f}\left(\frac{2r_0^2}{r_1^2} - \frac{4r^2 r_0^2}{r_1^4}\right) \tag{C.7}$$

Now, by assuming that:

$$\frac{OPD}{f} \ll 1 \text{and} \frac{(z-z_f)}{f} \ll 1 \tag{C.8}$$

the magnitude of the ratio is primarily governed by r_1, and more specifically by the minimum beam radius r_b. If one considers the "physical" minimum beam radius, the second term in parentheses may become significant. However, in the present practical application, the effective minimum radius governed by various phenomena like diffusion and internal reflection. By taking the minimum radius equal to the thermal diffusion radius, the second term always remains below 5%, and its contribution can be considered negligible.

Moreover, two important considerations mitigate its impact:

1. In the actual numerical implementation, we do not use the derivative form at all. Instead, we directly implement Eq. (3) with $r_1(z)$ computed at each integration point. The derivative derivation is purely theoretical and serves to justify the functional form of the heat source.
2. The excellent agreement between simulated and experimental fusion zone geometries (overlap>92% across all cases, Figs. 4, 5 and 6) and between predicted and measured peak temperatures (Fig. 9) confirms that any errors introduced by this simplification are negligible for engineering purposes.

Furthermore, as noted in Sect. 3.1, the effects of beam divergence are partially captured by the calibration of the plasma-related hyperparameters l_{00} and l_{02}, which account for plasma-induced defocusing at the top and bottom surfaces. Thus, the model remains physically consistent and accurate within its intended application range.

Another important aspect regards the averaging of wobble effects, which under some conditions may lead to important asymmetries that could not taken into account by our model. Therefore, it is worth to analyse under which conditions these approximations apply.

The approximation adopted in our model is supported by a comparison between the laser displacement during one wobbling period and the thermal diffusion length in the same time interval.

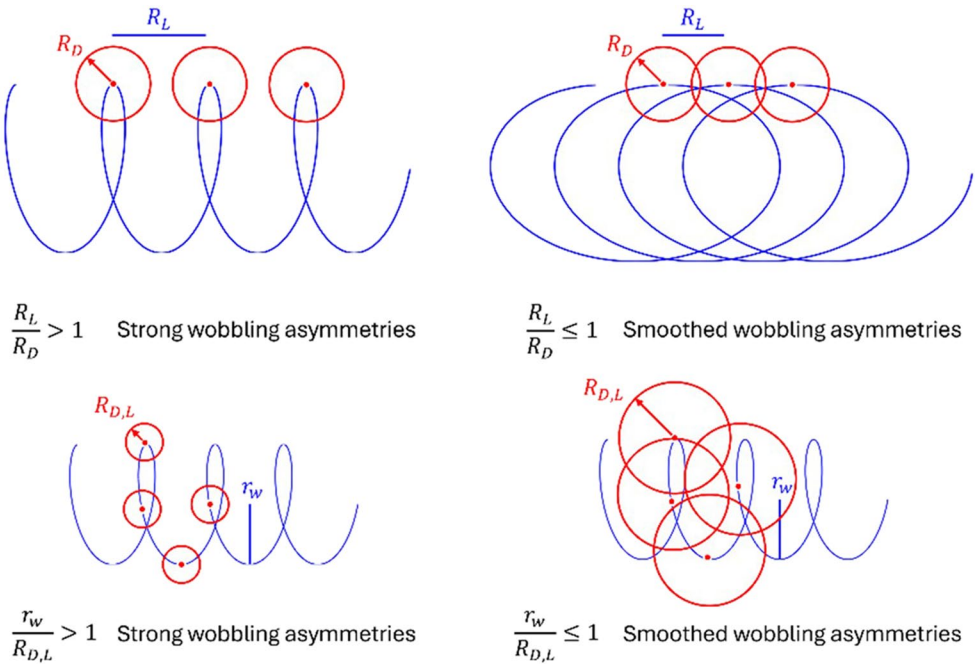

Fig. 13 Sketch of thermal scales with respect to wobbling scales as a function of the two parameters

The thermal diffusion length can be expressed as $R_D = \sqrt{D/f}$ where $f$is the wobble frequency while characteristic laser displacement during one oscillation period is $R_L = v/f$. The validity of the time-averaged approximation can therefore be assessed through the dimensionless ratio:

$$\frac{R_L}{R_D} = \frac{v}{\sqrt{Df}} \tag{C.9}$$

When $R_L/R_D \leq 1$, thermal diffusion is sufficiently rapid to smooth the spatial temperature variations induced by beam oscillation, thus justifying the use of an effective, time-averaged source. Conversely, for $R_L/R_D \gg 1$, periodic thermal asymmetries are expected, and a fully transient modeling approach would be required. In the present study, this ratio remains below 0.5 for all simulated conditions, indicating that thermal diffusion effectively smooths wobble-induced asymmetries within one oscillation period. This behaviour is also consistent with the experimentally observed melt pool symmetry.

Moreover, it is also relevant to consider a second dimensionless parameter that compares the imposed asymmetry length scale to the thermal diffusion length. In this case, the characteristic asymmetry length is the wobble radius r_w while the thermal scale should be evaluated with respect the laser velocity. The ratio can be written as:

$$\frac{r_w}{R_{D,L}} = \frac{r_w}{D/v_L} = \frac{r_w}{D} v_l$$

This parameter quantifies whether the spatial scale of the imposed oscillation is large enough to generate persistent asymmetries. When:

$$\frac{r_W}{R_{D,L}} \leq 1$$

thermal diffusion dominates over the geometrical asymmetry introduced by wobbling, leading to effective smoothing of temperature variations within one oscillation period. Conversely, values approaching or exceeding unity indicate that diffusion is not sufficient to homogenize the thermal field at the scale of the wobble radius, and transient asymmetries may develop. In our work, also this value is below 0.25, ensuring that asymmetries are thermally smoothed out. A sketch of both effects is shown in figure 13.

Author Contribution Paolo Ferro: Conceptualization, Methodology, Supervision, Writing – original draft, Writing – review & editing, Project administration, Funding acquisition
Riccardo Rossi: Conceptualization, Formal analysis, Visualization, Writing – original draft, Writing – review & editing
Alessandra Varone: Data curation, Resources, Experimental validation
Giuliano Angella: Review & editing
Franco Bonollo: Supervision, Review & editing
Fabio Bergamini: Welding trials and temperature measurements

Funding Open access funding provided by Università degli Studi di Padova within the CRUI-CARE Agreement. This work was supported by the PRIN 2022 project, ELAPSE: Laser Welding and Repair of Superalloys (project 20225YNH4M). ELAPSE is financed by the European Union through Italian PNRR funds.

Declarations

Competing interest The authors declare that they have no known competing financial interests or personal relationships that could have appeared to influence the work reported in this paper.

References

1. Cano-Salinas L, Salem M, Moussaoui K et al (2025) Laser metal deposition as repair technology for Inconel 718. Int J Adv Manuf Technol 136:2193–2208. https://doi.org/10.1007/s00170-024-14982-x
2. Bernhard R, Buchbender I, Wesling V, Kaierle S (2025) Single crystalline laser welding. In: Seume JR, Denkena B, Gilge P (eds) Regeneration of Complex Capital Goods. Springer, Cham, pp 207–222. https://doi.org/10.1007/978-3-031-51395-4_11
3. Dul I (2011) Application and processing of nickel alloys in the aviation industry. Weld Int 27:48–56. https://doi.org/10.1080/09507116.2011.600026
4. Zapiraina F, Zubiria F, Garciandía F, Tolosa I, Chueca S, Goiria A (2011) Development of laser welding of Ni-based superalloys for aeronautic engine applications (experimental process and obtained properties). Phys Procedia 12:105–112
5. Prakasha L, Kumar C, Gogai D, Kumar M, Devi S (2024) Laser beam welding of Inconel alloys: a review. J Phys : Conf Ser 2818:012047. https://doi.org/10.1088/1742-6596/2818/1/012047
6. Donnini R, Varone A, Palombi A, Spiller S, Ferro P, Angella G (2025) High energy density welding of Ni-based superalloys: an overview. Metals 15:30. https://doi.org/10.3390/met15010030
7. Kästner C, Neugebauer M, Schricker K, Bergmann JP (2020) Statistical analysis of pulsed laser beam welding repair strategies of nickel-base superalloys. Procedia CIRP 94:638–643. https://doi.org/10.1016/j.procir.2020.09.099
8. Wang H-S, Huang C-Y, Ho K-S, Deng S-J (2011) Microstructure evolution of laser repair welded René 77 nickel-based superalloy cast. Mater Trans 52:2197–2204. https://doi.org/10.2320/matertrans.M2011264
9. Romanin L, Ferro P, Fabrizi A, Berto F (2019) A metallurgical and thermal analysis of Inconel 625 electron–beam welded joints. Frattura Integrita Strutturale 50:251–263. https://doi.org/10.3221/IGF-ESIS.50.21
10. Vemanaboina H, Gundabattini E, Akella S, Rao ACUM, Buddu RK, Ferro P, Berto F (2021) Mechanical and metallurgical properties of CO_2 laser beam Inconel 625 welded joints. Appl Sci 11:7002. https://doi.org/10.3390/app11157002
11. Kocurek R, Adamiec J, Trans Tech Publ (2016) Mechanism of hot cracking welds of nickel alloy Inconel 625. Solid State Phenom 246:25–28. https://doi.org/10.4028/www.scientific.net/ssp.246.25
12. Liu M, Zhang Z (2019) Smoothed particle hydrodynamics (SPH) for modeling fluid-structure interactions. Sci China Phys Mech Astron 62:984701. https://doi.org/10.1007/s11433-018-9357-0
13. Trautmann M, Hertel M, Füssel U (2018) Numerical simulation of weld pool dynamics using a SPH approach. Weld World 62:1013–1020. https://doi.org/10.1007/s40194-018-0615-5
14. Li K, Guo X, Zhang J et al (2020) Simulation of deep penetration laser welding process by coupling smoothed particle hydrodynamics with ray–tracing scheme. Appl Therm Eng 179:115674. https://doi.org/10.1016/j.applthermaleng.2020.115674
15. Goldak J, Chakravarti A, Bibby M (1984) A new finite element model for welding heat sources. Metall Trans B 15:299–305. https://doi.org/10.1007/BF02667312
16. Patel VK, Patel JB, Patel KN (2018) Numerical simulation of transient temperature distribution in welding using Gaussian heat source model. J Manuf Process 32:136–146. https://doi.org/10.1016/j.jmapro.2018.03.019
17. Wang K, Li C, Zhang X (2020) Modelling and simulation of the weld pool shape and temperature distribution in laser welding using a volumetric Gaussian heat source. Opt Laser Technol 129:106312. https://doi.org/10.1016/j.optlastec.2020.106312
18. Ferro P, Bonollo F, Tiziani A (2010) Methodologies and experimental validations of welding process numerical simulation. Int J Comput Mater Sci Surf Eng 3:114–132. https://doi.org/10.1504/IJCMSSE.2010.033148
19. Ferro P, Berto F, Romanin L (2020) Understanding powder bed fusion additive manufacturing phenomena via numerical simulation. Frattura Integrita Strutt 14:252–284. https://doi.org/10.3221/IGF-ESIS.53.21
20. Ferro P, Tang K, Berto F, Salvati E (2024) Tuning residual stresses in welded structures by exploiting bio-inspired suture interfaces. Fatigue Fract Eng Mater Struct. https://doi.org/10.1111/ffe.14445
21. Vanini M, Searle S, Vanmeensel K, Vrancken B (2024) Avoiding heat source calibration for finite element modeling of the laser powder bed fusion process. Addit Manuf 92:104369. https://doi.org/10.1016/j.addma.2024.104369
22. Ye J, Khairallah SA, Rubenchik AM, Crumb MF, Guss G, Belak J, Matthews MJ (2019) Energy coupling mechanisms and scaling behavior associated with laser powder bed fusion additive manufacturing. Adv Eng Mater 21:1900185. https://doi.org/10.1002/adem.201900185
23. Krasnoperov MY, Pieters RRGM, Richardson IM (2004) Weld pool geometry during keyhole laser welding of thin steel sheets. Sci Technol Weld Join 9:501–506. https://doi.org/10.1179/136217104225021733
24. Kuryntsev SV, Gilmutdinov AK (2015) The effect of laser beam wobbling mode in welding process for structural steels. Int J Adv Manuf Technol 81:1683–1691. https://doi.org/10.1007/s00170-015-7312-y
25. Li J et al (2021) Analysis and improvement of laser wire filling welding process stability with beam wobble. Opt Laser Technol 134:106594. https://doi.org/10.1016/j.optlastec.2020.106594
26. Li K et al (2024) Effect of laser power on weld microstructure of AA6082 sheets remote laser welded by circular beam wobbling. Weld World 68:2761–2777. https://doi.org/10.1007/s40194-024-01802-9
27. Mukherjee T, Gao M, Palmer TA, DebRoy T (2023) Keyhole mode wobble laser welding of a nickel base superalloy – modeling, experiments, and process maps. J Manuf Process 106:465–479. https://doi.org/10.1016/j.jmapro.2023.10.017

28. Miyazaki Y, Katayama S (2013) Influence of laser–induced plume on penetration in laser welding. Q J Jpn Weld Soc 31:119–125. https://doi.org/10.2207/qjjws.31.119
29. Fabbro R, Slimani S, Doudet I, Coste F, Briand F (2006) Experimental study of the dynamical coupling between the induced vapour plume and the melt pool for Nd:YAG CW laser welding. J Phys D Appl Phys 39:394–398. https://doi.org/10.1088/0022-3727/39/2/023
30. Brock C, Hohenstein R, Schmidt M (2014) Mechanisms of vapour plume formation in laser deep penetration welding. Opt Lasers Eng 58:93–100. https://doi.org/10.1016/j.optlaseng.2014.02.001
31. Solomon A, Aravinthan G, Deepak R, Kishore Kumar M, Padmanaban MA (2018) Simulation and modeling of the effect of welding process parameters of Inconel 625. Int J Eng Res Technol 6:1–6